Multi-scale Modeling of the Heart Valve Interstitial Cell

Alex Khang, Daniel P. Howsmon, Emma Lejeune and Michael S. Sacks

Abstract Heart valve interstitial cells (VIC) are fibroblast–like cells that reside within the interstitium of heart valve leaflets. The biosynthetic activity of VICs is highly dependent upon the the mechanical demands of the extracellular environment. Thus, regular deformation of the leaflets throughout the cardiac cycle provides the mechanical stimulation that is necessary for VICs to maintain homeostasis of the valve and manage normal turnover of extracellular matrix constituents. When the deformation pattern of the VICs is altered during periods of growth or disease, VICs can undergo cellular activation and remodel the ECM of the valve to re-establish homeostasis. In order to better engineer treatments for heart valve diseases, it is of great importance to delineate the underlying mechanisms governing this crucial remodeling process. In this chapter, we present current experimental and computational modeling approaches used to study the complex multi-scale mechanical relationship between the valve leaflets and the underlying VICs. In addition, we discuss future directions toward modeling VIC signaling pathways and developing improved 3D multi-scale models of VICs.

A. Khang · D. P. Howsmon · E. Lejeune · M. S. Sacks (✉)
James T. Willerson Center for Cardiovascular Modeling and Simulation,
Institute for Computational Engineering and Sciences and the Department of Biomedical Engineering, The University of Texas at Austin, Austin, TX, USA
e-mail: msacks@ices.utexas.edu

A. Khang
e-mail: ak36582@utexas.edu

D. P. Howsmon
e-mail: daniel.howsmon@utexas.edu

E. Lejeune
e-mail: elejeune@utexas.edu

Y. Zhang (ed.), *Multi-scale Extracellular Matrix Mechanics and Mechanobiology*,
Studies in Mechanobiology, Tissue Engineering and Biomaterials 23,
https://doi.org/10.1007/978-3-030-20182-1_2

1 Introduction

Heart valves are dynamic living tissues whose physiological function is quite simple: to prevent the retrograde flow of blood within the heart. The mammalian heart has four valves: the aortic valve (AV), mitral valve (MV), pulmonary valve (PV), and tricuspid valve (TV). All valve leaflets are multi-layered structures composed of a heterogenous mixture of extracellular matrix (ECM) components with a specific structure that allows proper opening and closure of the valves. For instance, in the AV, the fibrosa layer contains mainly collagen and provides the majority of mechanical support in the valve while the ventricularis layer contains radially orientated elastin fiber networks that act as a low-energy recoiling mechanism during valve closure. In between these two layers, the spongiosa layer contains mainly proteoglycans and glycosaminoglycans that aid in compression of the valve leaflets during coaptation.

All valves undergo a complex time varying pattern of stretch and flexure that in turn deform the underlying valve interstitial cells (VIC). VICs are fibroblast-like mechanocytes that comprise $\sim$10 % of the total valve leaflet volume and respond to tissue-level stresses and deformations [5, 20]. In order to maintain the intricate and precise structure of the valve, VICs sense their mechanical environment and remodel the ECM constituents accordingly. In the quiescent state, VICs maintain the normal upkeep of ECM components to ensure valve homeostasis. During periods of both growth and disease, VICs are known to transition to an activated, myofibroblast-like phenotype, where they display increased contractility, prominent alpha smooth muscle actin (α-SMA) stress fibers, and increased ECM remodeling activity [4, 13]. VIC-ECM coupling is made possible through the VICs binding via integrins containing α and β subunits to ECM components such as fibronectin, laminin, and collagen [23, 43].

Remodeling of heart valve leaflet ECM can occur due to intrinsic and extrinsic factors. For instance, during pregnancy, the heart undergoes a drastic pressure overload, which drastically increases ventricular size and the mechanical loading of the MV [38]. Initially, this causes a reduction in collagen crimp which mechanically compresses the mitral VICs (MVICs). This in turn induces growth and remodeling mechanisms in an attempt to reestablish a normal homeostatic cell shape. It is thus hypothesized that in late pregnancy, homeostasis is reestablished through remodeling processes that decrease collagen fiber alignment and restore the collagen crimp, relieving the compression of MVICs.

Another example, for a diseased state, is ischemic MV regurgitation (IMR) which arises from cardiomyopathy and/or coronary heart disease that induces MV regurgitation as a secondary complication [7, 8]. This is driven by the displacement of papillary muscles, which assist in tethering the MV via chordae tendineae [21], during left ventricular (LV) remodeling. This process can cause the MV to dilate and prevent proper closing. To compensate, the MV enlarges and becomes stiffer through remodeling processes. Despite this, the MVICs fail to reestablish a homeostatic loading state within the MV because the altered loading patterns persist. As a result, MV repair and replacement procedures are commonly performed in these scenarios [1].

Pregnancy and IMR are two compelling examples of how tissue-scale mechanics can drive the cellular-scale deformation of MVICs and in turn induce drastic remodeling mechanisms. In the AV, calcific aortic valve disease (CAVD) is a major driver of aortic stenosis in elderly individuals and those with bicuspid aortic valves. During the onset of CAVD, AVICs form calcium nodules which drastically stiffen the valve leaflets, leading to stenosis. AV replacements with heterograft tissues or bioprosthetic valves are commonly performed to combat these symptoms.

These phenomena highlight the importance of multi-scale and holistic approaches to studying the mechanobiology of VICs and how the mechanobiology ultimately determines the tissue-level response of the valves. Despite our current understanding of the relationship between VIC mechanobiology and valve mechanics, little is known about the underlying cellular processes that govern it. In addition, little is known about layer-specific properties of VICs and how this connects to the formation of different valve layers with vastly different mechanical function [37]. In this chapter, we discuss current experimental and computational modeling techniques to study the mechanics of isolated VICs. We then go on to discuss the in-situ properties of VICs and preliminary investigations into layer-specific mechanical responses. We end by summarizing the use of synthetic hydrogel environments to study VIC mechanobiology and provide future directions towards developing cell signaling models that can be used to explain cellular mechanisms that allow for VIC regulation of valve ECM and refining existing models to more accurately elucidate VIC and ECM mechanical properties.

2 Isolated Cell Studies

2.1 Overview

Previous isolated cell studies have shown that VICs from the AV and MV are intrinsically stiffer than VICs from the PV and TV owing to the larger mechanical demands of the left side of the heart in which the AV and MV reside [33, 34]. In this more mechanically demanding environment, the VICs of the AV and MV undergo larger cytoplasmic and nuclear deformations which drives an up-regulation of α-SMA expression and subsequently increases VIC stiffness. In addition, VICs from the AV and MV display an up-regulation of ECM biosynthesis, resulting in thicker and stiffer valve leaflets overall.

Micropipette aspiration (MA) [34] and atomic force microscopy (AFM) [33] are valuable techniques that have been used to study the mechanics of isolated VICs. However, AFM measurements of VIC stiffness are 10–100 fold larger in magnitude than MA measurements. This is thought to be caused by the difference in internal stress fiber composition and architecture between free-floating, suspended VICs in MA experiments, and VICs seeded on a planar substrate in the AFM experiments. In suspension, VICs are thought to be in an inactivated state and do not express

prominent α-SMA fibers. This contrasts with VICs seeded on a 2D substrate that are in an activated state and therefore generate stronger contractile forces. In addition to the differences in VIC subcellular structures between the two tests, differences in effective stiffness values may arise because the organelles and cell structures are being measured at different length scales with each test. MA experiments measure a broader region on the cell while AFM is used to assess more local properties at the periphery or near the nucleus. A continuum mixture finite element model of an isolated VIC was developed to gain a better understanding of the role that organelles and especially stress fibers play in VIC effective stiffness.

2.2 Model Formulation

A first mechanical model of the VIC was developed through integrating the experimental data from both MA and AFM measurements on VICs from the AV (AVIC) and PV (PVIC) [39]. In the formulation of the model, consideration was given to the organelles most likely to contribute during a specific test. For example, during analysis of the MA results, the passive properties of both the basal cytoskeleton and cytoplasm (all organelles except for the stress fibers and the nucleus) and the stress fibers were thought to contribute the most and therefore their shear moduli were estimated from the MA data. Then, data from AFM measurements at the periphery of VICs and directly above the nucleus was used to calibrate the contractile strength of the α-SMA stress fibers and the shear modulus of the nucleus, respectively.

The finite element models were developed in the open source software FEBio [30]. In the MA simulations, the initial shape of the VIC was modeled as a sphere and the boundary between the cell and the micropipette was subjected to a contact–traction to induce friction-less sliding between the two surfaces [39]. In the AFM experiments, a representative VIC was modeled on a flat surface with two separate subdomains for the nucleus and the cytoplasm [40]. A no-slip boundary condition was applied on the bottom surface of the VIC and the contact between the VIC and the rigid indenter was modeled with a no-penetration, no-slip boundary condition.

2.2.1 Calibration of the Cytoplasm, Stress Fibers, and Nuclear Mechanics

The initial step in estimating the mechanical properties of the VIC uses MA data to extract the shear modulus of the cytoplasm (μ^{cyto}) and the stress fibers (μ^{sf}) (Fig. 1a). The total Cauchy stress $\mathbf{T}$ is the sum of both components

$$\mathbf{T} = \mathbf{T}_{cyto} + \mathbf{T}_{sf}\,. \tag{1}$$

The cytoplasm is modeled as a nearly incompressible, isotropic, hyperelastic material with a neoHookean material model with a transversely isotropic contribution from

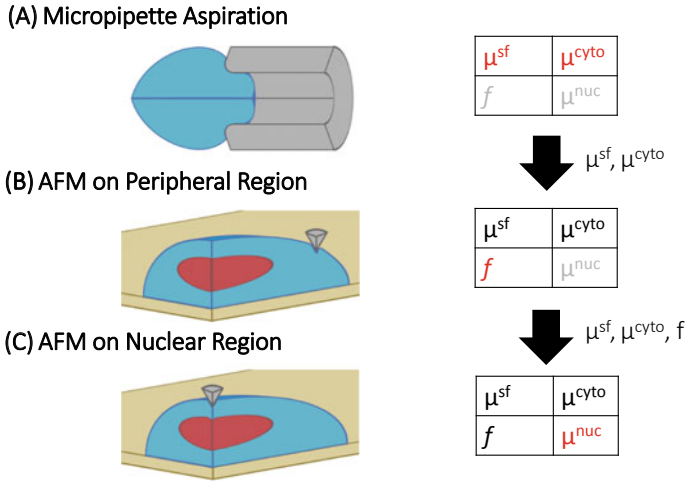

Fig. 1 **a** First, micropipette aspiration data is used to calibrate the shear modulus of the stress fibers (μ^{sf}) and the cytoplasm (μ^{cyto}). **b** Next, AFM measurements made at the periphery of VICs is used to estimate the stress fiber contraction strength (f). **C** Finally, AFM measurements made above the nuclear region are used to back out the shear modulus of the nucleus (μ^{nuc}). Figure adapted from [39]

the passive stress fibers. The full explicit Cauchy stress used to analyze the MA data is as follows

$$\mathbf{T} = 2\frac{1}{J}\mathbf{F}\frac{\partial}{\partial \mathbf{C}}\left[\frac{\mu^{cyto}}{2}(\bar{I}_1 - 3) + \frac{1}{2}K(\ln J)^2\right]\mathbf{F}^T + \frac{1}{4\pi}\int_0^{2\pi}\int_0^{\pi}\left[H(I_4 - 1)2\frac{I_4}{J}\frac{\partial}{\partial I_4}\left(\frac{\mu^{sf}\bar{\phi}^{sf}}{2}(I_4 - 1)^2\right)\mathbf{m}\otimes\mathbf{m}\right]\sin\theta\, d\theta d\phi. \tag{2}$$

where $\bar{I}_1 = J^{\frac{-2}{3}}I_1$, I_1 is the first invariant of the deformation gradient tensor $\mathbf{F}$ ($I_1 = \text{tr}(\mathbf{F})$), J is the jacobian ($J = \det(\mathbf{F})$), $\mathbf{C}$ is the right Cauchy-Green deformation tensor ($\mathbf{C} = \mathbf{F}^T\mathbf{F}$), K is the bulk modulus, H is a heavy side step-function introduced to enforce the passive stress that only arises from the fiber stretch, I_4 is the stress fiber stretch along the initial direction $\mathbf{m}_0$, $\mathbf{m}$ is the current state of the fibers initially oriented along $\mathbf{m}_0$ ($\mathbf{m} = \lambda^{-1}\mathbf{F}\cdot\mathbf{m}_0$, where $\lambda = \sqrt{I_4}$), and $\bar{\phi}^{sf}$ is the normalized α-SMA expression level. Direction $\mathbf{m}_0$ is characterized using two angles: $\theta \in [0, \pi]$ and $\phi \in [0, 2\pi]$ and $\mathbf{m}_0(\theta, \phi) = \sin\theta\cos\phi\mathbf{e}_1 + sin\theta\sin\phi\mathbf{e}_2 + \cos\theta\mathbf{e}_3$ where $\mathbf{e}_1$, $\mathbf{e}_2$, and $\mathbf{e}_3$ are the unit normal basis vector for the Cartesian coordinates. The parameters μ^{cyto} and μ^{sf} are determined through minimization of the least square error between the simulated and experimental aspiration lengths with respect to the applied aspiration pressure of the VICs in the MA experiments.

During the analysis of AFM experimental results, the properties of the stress fiber contraction strength and the nucleus are incorporated into the total Cauchy stress (Fig. 1b, c) as:

$$\mathbf{T} = \mathbf{T}_{cyto} + \mathbf{T}_{sf} + \mathbf{T}_{f} + \mathbf{T}_{nuc}. \tag{3}$$

First, AFM results from measurements performed on the periphery of VICs are used to find the contraction strength (f) of the stress fibers with the following expanded equation of the total Cauchy stress:

$$\begin{aligned}\mathbf{T} = {} & 2\frac{1}{J}\mathbf{F}\frac{\partial}{\partial \mathbf{C}}\left[\frac{\mu^{cyto}}{2}(\bar{I}_1 - 3) + \frac{1}{2}K(\ln J)^2\right]\mathbf{F}^T \\ & + \int_0^{2\pi}\int_0^{\pi}\left[\Gamma_t(\mathbf{m})H(I_4 - 1)2\frac{I_4}{J}\frac{\partial}{\partial I_4}\left(\frac{\mu^{sf}\bar{\phi}^{sf}}{2}(I_4 - 1)^2\right)\mathbf{m}\otimes\mathbf{m}\right]\sin\theta\, d\theta d\phi. \\ & + \int_0^{2\pi}\int_0^{\pi}\left[\Gamma_t(\mathbf{m})f\cdot\bar{\phi}^{sf}\frac{I_4}{J}\mathbf{m}\otimes\mathbf{m}\right]\sin\theta\, d\theta d\phi.\end{aligned} \tag{4}$$

where $\Gamma_t(\mathbf{m})$ is the constrained von-Mises distribution [17] which represents the stress fiber orientation distribution with respect to $\mathbf{m}$, the current fiber direction. Then, the shear modulus of the nucleus μ^{nuc} was determined by using AFM data from measurements made above the nucleus and through the following equation for Cauchy's stress:

$$\mathbf{T} = 2\frac{1}{J}\mathbf{F}\frac{\partial}{\partial \mathbf{C}}\left[\frac{\mu^{nuc}}{2}(\bar{I}_1 - 3) + \frac{1}{2}K(\ln J)^2\right]\mathbf{F}^T. \tag{5}$$

The parameters f and μ^{nuc} are calibrated through minimization of the least square error between the experimental and simulated indentation depth with respect to applied force at the cell periphery and above the nucleus, respectively.

From the constitutive model (Eqs. 4 and 5), the shear modulus of the cytoplasm, stress fibers, the nucleus and the stress fiber contraction strength (f) are determined (Table 1). The model predicts that the intrinsic stiffness of the cellular subcomponents is conserved between VICs from the AV and PV. However, a drastic difference in the contraction strength between AVICs and PVICs is predicted. AVIC contraction strength is reported to be ~10 times stronger than PVIC contraction, reinforcing that the stiffness of VICs is positively correlated with α-SMA expression levels [34]. This is consistent with the previous discussion of why AFM measurements are 10–100 fold larger than MA measurements.

Table 1 Parameter values determined from the constitutive model for both AVICs and PVICs. Table adapted from [39]

	μ^{cyto} (Pa)	μ^{sf} (Pa)	f (kPa)	μ^{nuc} (kPa)
AVIC	5	390	35.27 ± 3.42	15.64 ± 2.46
PVIC	5	390	3.86 ± 0.61	16.06 ± 2.19

2.2.2 Incorporation of Stress Fiber Force-Length Relations, Expression Levels, and Strain Rate

In an extended mechanical model of the VIC [40], stress fiber force-length relations, expression levels of F-actin and α-SMA stess fibers, and the strain rate sensitivity of VICs in response to AFM indentation are incorporated. Briefly, VICs were seeded onto 2D collagen coated cover slips and were subjected to five separate treatments before AFM measurements were made:

1. **CytoD**: Cytochalasin D was used to disassemble the actin fiber network of the VICs. This group served as a negative control.
2. **C5 and C90**: The C5 VIC group was subjected to testing within 5 mM potassium chloride (KCl) to emulate normal physiological conditions. The C90 group was tested within 90 mM KCl (induces cell activate contraction) and is representative of a hypertensive cell state. These groups served as a negative control for the TGF-β1 group to follow.
3. **T5 and T90**: TGF-β1 is a potent cytokine that effectively induces the activation of VICs and has been shown to lead to complications in vivo such as calcification and valve stenosis [12, 36]. TGF-β1 has been shown to induce VICs to transition to a myofibroblast-like phenotype which increases α-SMA expression and contractility. The T5 group is treated with both TGF-β1 and 5 mM KCl to allow for measurements on VICs in the myofibroblast state and under normal conditions. The T90 group is treated with TGF-β1 and 90 mM KCl to study myofibrolast-like VICs in a hypertensive state.

For model formulation and subsequent analysis of the AFM results, the F-actin and α-SMA stress fiber expression levels of the VICs under each chemical treatment group were quantified from analyzing fluorescence images (Fig. 2a, b). Only α-SMA stress fibers that co-localized with F-actin stress fibers are considered to avoid accounting for α-SMA subunits that exist within the cytoplasm and do not contribute to active contraction. Consistent with the first pass model, the total Cauchy stress is taken to be the sum of the contributions from the cytoplasm and the stress fibers (Eq. 1). The cytoplasm is modeled as a nearly incompressible neo-Hookean material as follows:

$$\mathbf{T}^{cyto} = 2\frac{1}{J}\mathbf{F}\frac{\partial}{\partial \mathbf{C}}\left[\frac{\mu^{cyto}}{2}(\bar{I}_1 - 3) + \frac{1}{2}K(\ln J)^2\right]\mathbf{F}^T. \tag{6}$$

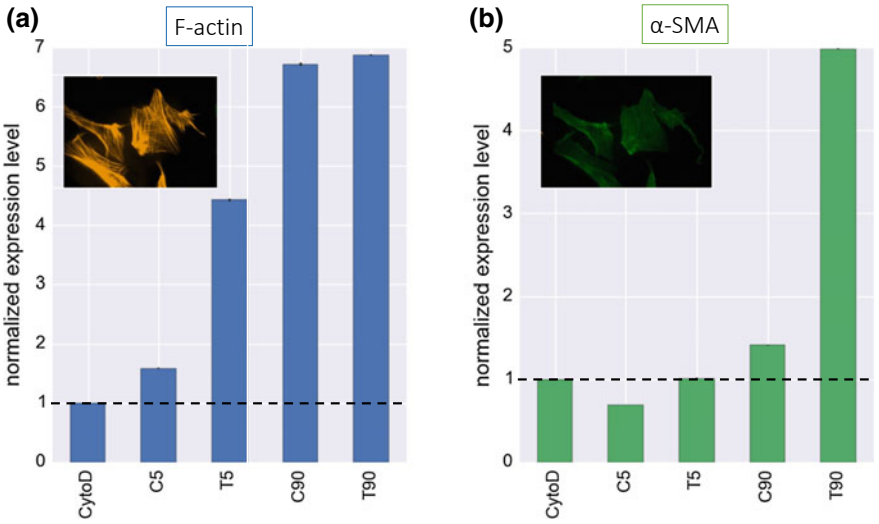

Fig. 2 **a** F-actin expression levels of VICs with respect to the chemical treatment conditions. **b** Expression level of α-SMA stress fibers that co-localize with F-actin fibers under the different chemical treatments. Figure adapted from [40]

The stress fibers were modeled as

$$\mathbf{T}^{sf} = \frac{1}{\mathbf{J}}\mathbf{F}\left[\int_{-\frac{\pi}{2}}^{\frac{\pi}{2}} \Gamma(\mathbf{m}_0)[H(I_4-1)T^p(\mathbf{m}_0) + T^a(\mathbf{m}_0) + T^v(\mathbf{m}_0)] \times (\mathbf{m}_0 \otimes \mathbf{m}_0) d\theta\right]\mathbf{F}^T \tag{7}$$

where $\mathbf{m}_0$ defines the inital direction of the stress fibers and T^p, T^a, and T^v are the one dimensional passive, active, and viscous contributions to stress, respectively. The passive component of the stress fibers are captured by

$$T^p = 2\mu_{sf}\bar{\phi}_{F-actin}(I_4 - 1) \tag{8}$$

where μ_{sf} is the shear modulus of the stress fibers and $\bar{\phi}_{F-actin}$ is the expression level of F-actin (Fig. 2a). The active portion of the stress fibers is modeled as

$$T^a\left(\bar{\phi}_{\alpha-SMA}, \bar{\phi}_{F-actin}, \lambda\right) = f_0\left(\bar{\phi}_{\alpha-SMA}, \bar{\phi}_{F-actin}\right) f_1(\lambda) \tag{9}$$

where f_0 is the maximum amount of contraction possible and is a function of the α-SMA and F-actin expression levels (Fig. 2a and b), and f_1 is the length-tension relationship which is a function of the stretch (λ). The maximum contraction is thus modeled as:

$$f_0\left(\bar{\phi}_{\alpha-SMA}, \bar{\phi}_{F-actin}\right) = f_{\alpha-SMA}\bar{\phi}_{\alpha-SMA} + f_{F-actin}\bar{\phi}_{F-actin}, \tag{10}$$

where $f_{\alpha-SMA}$ and $f_{F-actin}$ are the contraction strength of each stress fiber per unit expression level and are kept constant regardless of activation level. The length-tension relation is adapted from [44] and is implemented as:

$$\begin{aligned} f_1(\varepsilon, \varepsilon_0, \varepsilon^*) &= \exp -((\varepsilon - \varepsilon^*)/\varepsilon_0)^2 \\ \varepsilon &= (I_4 - 1)/2 \end{aligned} \tag{11}$$

where ε is the fiber strain, ε^* is the strain level where maximum contraction occurs, and ε_0 is the rate of decay of the contractile strength with respect to ε^*. From simulation, it is noted that the value of ε^* had no substantial effect on the results when $|\varepsilon^*| < \varepsilon_0$. Therefore ε^* and ε_0 are set to 0 and 0.1, respectively, producing a similar length-tension relationship to one used previously to model muscle fiber contraction [15, 44]. From the indentation experiments, it is noted that the stiffness of the VICs is highly dependent upon levels of α-SMA. Thus, it is assumed that the viscous response of the stress fibers should be related to the viscosity of α-SMA ($\eta_{\alpha-SMA}$), α-SMA expression level, and strain rate ($\dot{\varepsilon}$) as follows:

$$T^v = \eta_{\alpha-SMA}\bar{\phi}_{\alpha-SMA}\dot{\varepsilon}. \tag{12}$$

In its entirety, the updated constitutive model of the VIC is as follows:

$$\begin{aligned} \mathbf{T} = {} & 2\frac{1}{J}\mathbf{F}\frac{\partial}{\partial \mathbf{C}}\left[\frac{\mu^{cyto}}{2}(\bar{I}_1 - 3) + \frac{1}{2}K(\ln J)^2\right]\mathbf{F}^T \\ & + \frac{1}{J}\mathbf{F}[\int_{\theta_p-\frac{\pi}{2}}^{\theta_p+\frac{\pi}{2}} \Gamma(\mathbf{m}_0)[H(I_4 - 1)2\mu_{sf}\bar{\phi}_{F-actin}(I_4 - 1) \\ & + f_0\left(\bar{\phi}_{\alpha-SMA}, \bar{\phi}_{F-actin}\right)f_1(\lambda) + \eta_{\alpha-SMA}\bar{\phi}_{\alpha-SMA}\dot{\varepsilon}] \\ & \times (\mathbf{m}_0 \otimes \mathbf{m}_0)d\theta]\mathbf{F}^T. \end{aligned} \tag{13}$$

where the first term represents the contributions of the cytoplasm, and the second through fourth terms are the passive, active contraction, and viscous contributions of the stress fibers, respectively.

2.3 Model Results

The system of partial differential equations presented previously was incorporated into FEBio to simulate the MA and AFM experiments (Fig. 3a and b). All parameters of interest were computed using non-linear least squares with the Levenberg-Marquardt algorithm to match the experimental and simulated indentation depth versus force data obtained from AFM measurements. From the constitutive model, the shear modulus (μ_{sf}), contraction strength (f_0), and viscosity ($\eta_{\alpha-\mathrm{SMA}}$) of the stress fibers are determined. From this, the total stress fiber shear modulus

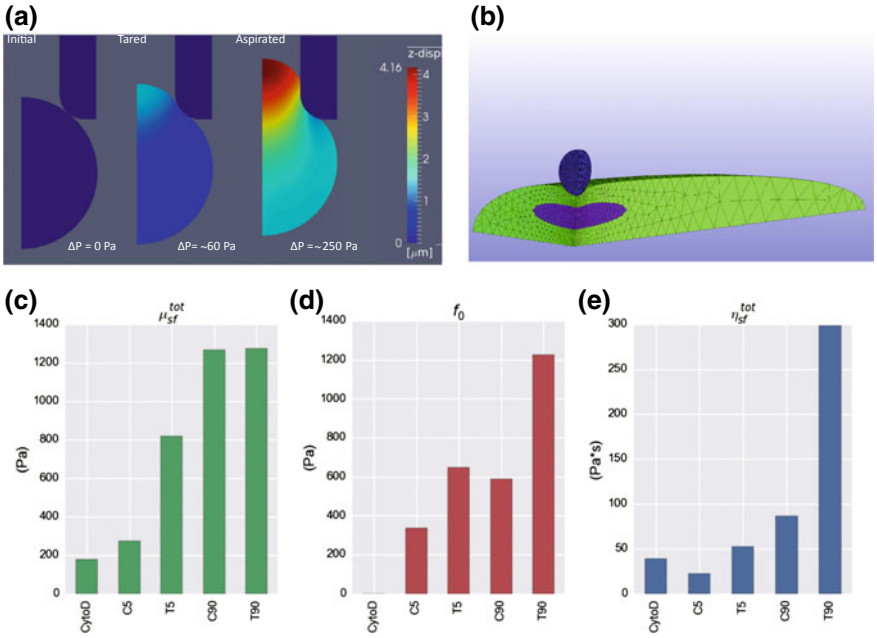

Fig. 3 Finite element models of the **a** MA and **b** AFM experiments, respectively. The **c** total shear modulus (μ_{sf}^{tot}), **d** contraction strength (f_0), and **e** total viscosity (η_{sf}^{tot}) of the stress fibers for each treatment condition. Higher expression of α-SMA in the T90 group largely increases the contraction strength and viscosity of the stress fibers. Figures taken from [39, 40]

($\mu_{sf}^{tot} = \mu_{sf}\bar{\phi}_{F-actin}$) and total viscosity of the stress fibers ($\eta_{sf}^{tot} = \eta_{\alpha-SMA}\bar{\phi}_{\alpha-SMA}$) are easily computed (Fig. 3c–e).

Results of the simulation clearly show that as VICs become more activated, the contraction strength (f_0) of the stress fibers increases (Fig. 3d). In addition, the viscosity of the stress fibers increases drastically (Fig. 3e, T90 group). This finding indicates that the difference in mechanical response when VICs in the T90 group were subjected to fast and slow strain rates (Fig. 4) is due to an increase in α-SMA stress fiber viscosity. No strain-rate sensitivity was observed in any of the other treatment groups.

The computed contraction strength (f_0) is found to be non-zero for the C5, T5, C90, and T90 groups (Fig. 3d). From these values, the contractile force arising separately from α-SMA and F-actin stress fibers is calculated using Eq. 10, resulting in four linear equations and two unknowns. From this, $f_{\alpha-SMA}$ and $f_{F-actin}$ are estimated to be 96.8 and 76.7 Pa, respectively. This result indicates that the incorporation of α-SMA in the stress fibers increases the contraction of VICs, consistent with previously reported experimental findings [10, 19, 31, 46]. The separate contributions of F-actin and α-SMA stress fibers to the overall contraction strength the estimated total contraction strength (f_0), and the expression levels of α-SMA ($\bar{\phi}_{\alpha-SMA}$) and F-actin ($\bar{\phi}_{F-actin}$) are computed by using Eq. 10 (Fig. 5). It is observed that within

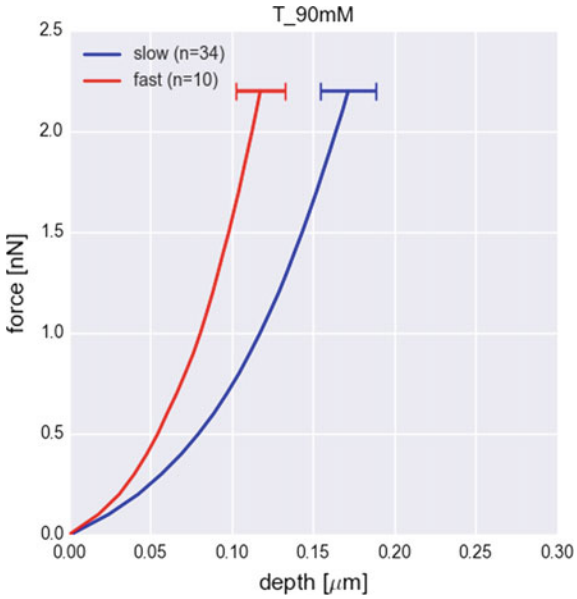

Fig. 4 Indentation depth versus force plots from AFM measurements performed on VICs within the T90 treatment group. Strain rate sensitivity is only observed within this group. The model predicts that an increase in the total viscosity of the α-SMA fibers (η_{sf}^{tot}) is likely the source of the observed strain-rate sensitivity. Figure adapted from [40]

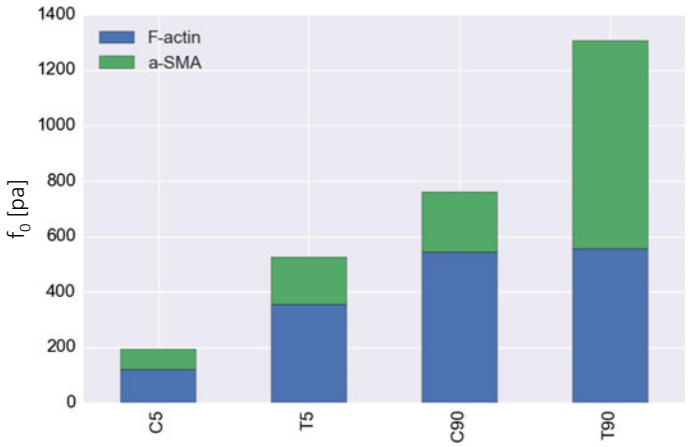

Fig. 5 The contributions of F-actin and α-SMA stress fibers to the overall estimated contraction strength. Note how every group contains contributions from both stress fibers but the T90 group is largely dominated by the effects of α-SMA. Figure taken from [40]

each treatment group, both F-actin and α-SMA stress fibers contributed to the overall contraction strength. However, in the T90 group, the contribution from α-SMA dominates the contraction strength due to the higher level of VIC activation in this group.

2.4 Conclusions

Mechanical assessment of isolated cells provided valuable insight into the differences between VICs under different conditions. Combining experimental techniques with computational models explains why these differences exist. Namely, the computational models are able to attribute the difference in stiffness between AVICs and PVICs to an increase in expression of α-SMA which leads to an increase in total stress fiber contraction strength. Furthermore, computational models of the VIC are able to delineate the separate contributions of F-actin and α-SMA to the total stress fiber contraction strength under different activation levels.

3 A Macro-micro Modeling Approach for the Down-Scale Estimation of AVIC Mechanics

3.1 Overview

Studying isolated VICs provides valuable insight into how VIC activation and increased expression levels of α-SMA alter the VIC biophysical state. However, these techniques are limited because they require VICs to be studied either on 2D glass coverslips or in suspension. These environments are not representative of the native cellular milieu and fail to elicit accurate in-situ VIC response.

Using native valve tissue to study VIC mechanics offers an alternative method to isolated cell studies. Native tissue is an attractive tool because of its physiological relevance and the availability of animal models. Previously, Merryman et al. showed that VIC contraction has a direct effect on the bending stiffness of AV leaflets and that the bending response of AV tissue is direction dependent [32]. In addition, Merryman et al. showed that when bent against the natural leaflet curvature, AVIC contraction had a larger effect on the overall bending stiffness of the leaflet compared to being bent in the direction of the natural leaflet curvature. Although these experimental results are insightful, it is difficult to delineate the underlying causes. Thus, the development of computational models is needed to further our understanding of the role that the underlying AVICs play in AV micromechanics. However, the AV leaflet tissue does not satisfy conventional multi-scale requirements due to the similarity in scale between the average leaflet thickeness (500 μm) and the average size of an AVIC (15 μm). This similarity in scale (10:1) is not appropriate for multi-scale

modeling methods and thus an alternative approach must be utilized. To circumvent these issues, a macro-micro modeling approach is established to directly map the boundary conditions on the macro level to the micro level.

3.2 Summary of Experimental Methods

Fresh native porcine AV leaflets were excised and subjected to three-point bending tests (Fig. 6a, b) [32]. Each leaflet was tested under normal, hypertensive, and inactive conditions. This was done by incubating the test specimens within 5 mM KCl, 90 mM of KCl, and thapsigargin (a known potent inhibitor of calcium ATPase), respectively. From the tests, moment versus curvature plots (M/I vs. $\Delta\kappa$) are generated. Then, the effective stiffness (E_{eff}) of the leaflets under each contractile level and with respect to testing with the natural leaflet curvature (WC - ventricularis under tension and fibrosa under compression) and against the natural leaflet curvature (AC - fibrosa under tension and ventricularis under compression) are calculated using the Euler-Bernoulli relation as follows:

$$\frac{M}{I} = E_{eff}\,\Delta\kappa \tag{14a}$$

$$E_{eff} = \frac{M}{I\,\Delta\kappa}. \tag{14b}$$

Values of E_{eff} calculated from Eqs. 14a and 14b for the AV leaflet test specimens are reported in Fig. 6c.

From the experimental results, it was noted that only in the AC direction showed a substantial increase in E_{eff} after treatment with 90 mM KCl (Fig. 6b). In addition, a decrease in E_{eff} was noted in all groups treated with thapsigargin, which completely inhibits the contraction of the underlying AVICs. Although these experimental results provide insight into how AVIC contraction modulates the flexural stiffness of the AV leaflet, they fail to meaningfully delineate the underlying mechanisms that cause a drastic change in E_{eff} in the AC curvature direction. In addition, they fail to elucidate the lack of significant changes observed in the WC direction despite treatment with 90 mM KCl. To further investigate the underlying phenomenon responsible for this behavior, a finite-element model of the bending experiment is developed and the displacements of the macro level representative volume element (RVE) are mapped to a refined micro level RVE to determine the underlying parameters that govern AVIC in-situ contractile effects on AV leaflet flexural stiffness [2].

3.3 Macro Model Formulation

Previously, it has been shown that the spongiosa layer behaves mechanically as a contiguous extension of the fibrosa and ventriculars layers [3]. Therefore, the

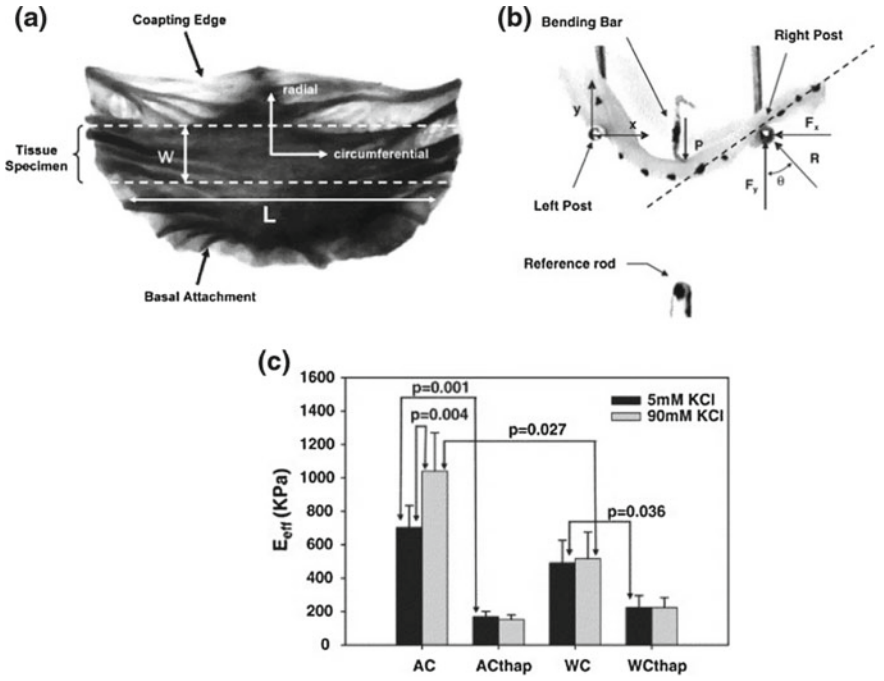

Fig. 6 **a** An excised AV leaflet. The test specimens were consistently excised just below the nodulus of Arantus. **b** Photograph of an AV test specimen undergoing three-point bending. **c** The effective stiffness (E_{eff}) of the AV leaflets before (5 mM KCl) and after (90 mM KCl) exposure to the active contraction treatment under normal (no thapsigargin) and inactive (thapsigargin) conditions. E_{eff} of the leaflets not treated with thapsigargin increased drastically in the AC direction after treatment with 90 mM KCl. The introduction of thapsigargin decreased E_{eff} in all groups. Figure adapted from [32]

AV leaflet is modeled as a bilayer, bonded beam with the finite-element software ABAQUS (Dassault Systemes, Johnston, RI, USA) using brick elements. Both layers were assigned a bimodular neo-Hookean isotropic nearly incompressible material model as follows:

$$W^d = \frac{{}_{state}\boldsymbol{\mu}^{l,d}_{Macro}}{2}(I_1 - 1) - p(I_3 - 1) \tag{15}$$

where ${}_{state}\boldsymbol{\mu}^{l,d}_{Macro}$ is the state dependent shear modulus of the layer (l = fibrosa (F) or ventricularis (V)) with respect to the testing direction (d = under tension (+) or compression (−)), $\mathbf{I}_3 = det(\mathbf{C})$ is the third invariant of the right Cauchy-Green deformation tensor, and p is the Lagrange multiplier that enforces incompressibility. The macro-level simulation boundary conditions are a pin constraint at the left edge of the specimen with small and controlled displacements in the x-direction applied at the right edge of the specimen. The dimensions of the simulated geometry are

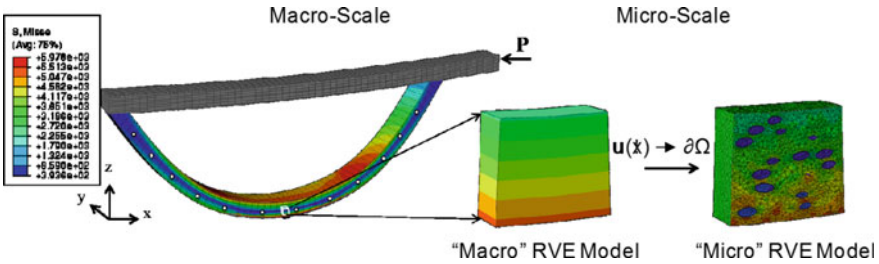

Fig. 7 Macro-level FE simulation of the bending experiments. The displacements of the "Macro" RVE model are mapped as boundary conditions to the "Micro" RVE model. Figure taken from [2]

kept consistent with that of the experimental test specimens (15 mm × 4 mm × 0.462 mm). The bilayer is divided in the thickness direction as 60 % fibrosa and 40 % ventricularis based on measurements from native AV tissue [5] (Fig. 7).

3.4 Macro Model Parameter Estimation

The tissue parameters are estimated using the experimental bending data. From a previous study [3], the moduli ratios for each layer under tension and compression were determined and used to estimate the inactive tissue parameters by fitting the FE simulation in the WC and AC bending directions simultaneously. The simulated moment-curvature plots are generated using the nodal locations along the edge of the geometry and the resulting reaction force on the left side of the geometry due to end displacement.

Next, the tissue parameter estimation for both the hypertensive and normal cases is performed. It is assumed that under compression, AVICs do not contribute to the stiffening of the valve tissues due to lack of tension from the surrounding ECM, an integral component needed for actin filament assembly and thus cell contraction. Therefore, the inactive compressive moduli are held constant and the tensile moduli are determined for both layers under normal and hypertensive conditions by fitting the simulated results to the experimental data for the AC and WC cases. Twelve total parameters are estimated from the macro RVE model (2 (layers) × 2 (tensile and compressible moduli) × 3 (each contractile state - "inactive", "normal", and "hyper") = 12 total parameters) and are reported in Table 2.

3.5 Micro Model Formulation

The micro model contains discrete ellipsoidal AVIC inclusions with distribution, size, and density determined from histological slices (Fig. 8) [5, 20]. The AVICs are modeled using a prolate spheroid, and are 14.16 μm long and 7.49 μm wide. The

Table 2 Estimated tissue parameters for each layer in tension and compression and under inactive, normal, and hypertensive contractile states. In addition, goodness of fit to the experimental data (R^2) as well as thickness normalized (0 = start of ventricularis, 1 = end of fibrosa) neutral axis locations (where axial stretch = 1) are reported for each activation state and test direction. Table taken from [2]

Activation state	Layer	μ^{+}_{Macro}	μ^{-}_{Macro}	Tension/compression Layer Moduli Ratios	R^2	Neutral axis (WC)	Neutral axis (AC)
Inactive	F	206.42	43.76	~5:1	0.990	0.36	0.75
	V	96.19	24.77	~4:1			
Normal	F	1496.67	43.76	~34:1	0.998	0.28	0.87
	V	311.93	24.77	~13:1			
Hyper	F	2250.78	43.76	~51:1	0.989	0.28	0.88
	V	311.93	24.77	~13:1			

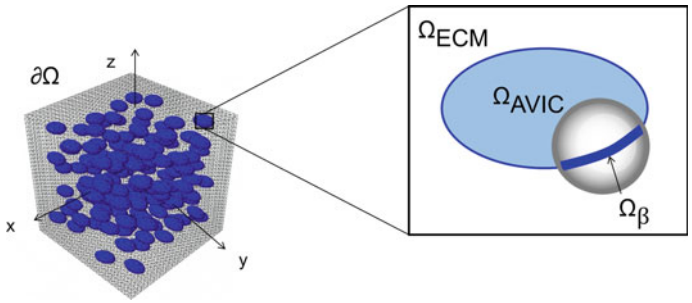

Fig. 8 Mico RVE model with ellipsoidal AVIC inclusions. Ω_{ECM}, Ω_{AVIC}, and Ω_{β} represent the sub-domains of the ECM, AVIC, and inter-facial boundary, respectively. $\delta\Omega$ represents the boundary of the domain facing outwards. Figure taken from [2]

density of the AVICs is kept consistent with native tissues at 270 million AVICs per ml, and the AVICs are assigned a preferred direction along the circumferential axis and are oriented at normally distributed angles of 9.7° and 5.3°.

3.5.1 Modeling of the ECM Subdomain

The micro RVE model is divided into three subdomains: the ECM (Ω_{ECM}), the AVICs (Ω_{AVIC}), and the boundary between the two (Ω_{β}) (Fig. 8). A neo-Hookean material model is used to model the ECM subdomain (Ω_{ECM}) with the Cauchy stress defined by

$$\mathbf{T} = 2\frac{1}{J}\mathbf{F}\frac{\partial}{\partial \mathbf{C}}\left[\frac{\mu^{l,d}_{micro}}{2}(\bar{I}_1 - 3) + \frac{1}{2}K(\ln J)^2\right]\mathbf{F}^T. \tag{16}$$

3.5.2 Modeling of the AVIC Subdomain

For the AVIC subdomain (Ω_{AVIC}), a modified version of the VIC mechanical model formulated from the isolated cell studies discussed in the earlier section is used with a combined Cauchy stress of

$$\mathbf{T} = \mathbf{T}_{cyto} + \mathbf{T}_{sf} + \mathbf{T}_{active} \tag{17}$$

where $\mathbf{T}_{cyto}$, $\mathbf{T}_{sf}$, and $\mathbf{T}_{active}$ are contributions from the cytoplasm, passive stress fibers, and active contractile response of the stress fibers, respectively. The constitutive model used for the isolated VIC (Eq. 13) was adapted to remove any contributions from the viscous effects of the stress fibers since strain rate studies were not performed under bending. The final AVIC constitutive model is as follows:

$$\begin{aligned}\mathbf{T} = {} & 2\frac{1}{J}\mathbf{F}\frac{\partial}{\partial \mathbf{C}}\left[\frac{\mu_{cyto}}{2}(\bar{I}_1 - 3) + \frac{1}{2}K(\ln J)^2\right]\mathbf{F}^T \\ & + \frac{1}{J}\mathbf{F}\Bigg[\int_0^{2\pi}\int_0^{\pi}\Gamma(\mathbf{m}_0(\psi,\theta))H(I_4 - 1)2\mu_{sf}\bar{\phi}_{F-actin}(\mathbf{I}_4 - 1) \\ & \qquad \mathbf{m}_0(\psi,\theta)\otimes\mathbf{m}_0(\psi,\theta)\sin\psi\, d\psi\, d\theta\Bigg]\mathbf{F}^T \\ & + \frac{1}{J}\mathbf{F}\left[\int_0^{2\pi}\int_0^{\pi}\Gamma(\mathbf{m}_0(\psi,\theta))f_0 f_I(\lambda)\mathbf{m}_0(\psi,\theta)\otimes\mathbf{m}_0(\psi,\theta)\sin\psi\, d\psi\, d\theta\right]\mathbf{F}^T.\end{aligned} \tag{18}$$

A π periodic von Mises distribution [29] (the 3D counterpart to the constrained von-Mises distribution used for the isolated VIC models [39, 40]) is used to model the 3D stress fiber orientation distribution. The function takes the form:

$$\Gamma(b, \mathbf{m}) = \frac{1}{\pi}\sqrt{\frac{b}{2\pi}}\frac{\exp(2bm_1^2)}{\mathrm{erfi}(\sqrt{2b})} \tag{19}$$

where $\mathbf{m} = (m1, m2, m3)$ is the orientation vector of the stress fibers and $b > 0$ is a shape concentration parameter. The function erfi is defined as

$$\mathrm{erfi}(b) = -i\,\mathrm{erf}(ib) = \frac{2}{\sqrt{\pi}}\int_0^b \exp(t^2)dt. \tag{20}$$

Only the case in which b is real is considered. This produces a transversely isotropic fiber orientation because Eq. 19 only contains the first component of $\mathbf{m}$ (i.e. m_1). In Eq. 20, the parameter b is tunable such that the lower limit produces an isotropic orientation ($b = 0$) and the upper limit produces a completely one dimensional orientation ($b = \infty$).

3.5.3 Modeling of the Boundary Interface

The complete microstructure of each layer is not explicitly modeled due to lack of feasibility and computational cost. Instead, a thin interface boundary (Ω_β) around every AVIC inclusion is incorporated to allow for the control of the AVIC-ECM connectivity level. This boundary is 0.650 μm in thickness and is modeled using explicit boundary elements that replaced a small volume of the ECM around each AVIC. The interface boundary is modeled with the following constitutive equation

$$\mathbf{T} = 2\frac{1}{J}\mathbf{F}\frac{\partial}{\partial \mathbf{C}}\left[\frac{(\beta^l_{AVIC})(\mu^{l,d}_{micro})}{2}(\bar{I}_1 - 3) + \frac{1}{2}K(\ln J)^2\right]\mathbf{F}^T. \tag{21}$$

When $\beta^l_{AVIC} = 1$, the AVICs are completely connected to the ECM and the interface boundary has the same mechanical properties as the ECM. As β^l_{AVIC} approaches 0, the softer interfacial layer causes the AVICs to become less connected to the ECM.

3.6 Macro and Micro Model Homogenization Scheme

After the tissue scale parameters are determined from the macro RVE model, the displacements of the RVEs from each layer are mapped to the micro RVE model as boundary conditions (Fig. 7). This essentially imposes a boundary value problem on the micro model. The parameters within the micro model are then determined by minimizing the difference in the von Mises stress index between the macro and micro RVE models to maintain continuity between them using

$$\overline{T}^{VM}_{MacroRVE} = \sqrt{\frac{3}{2}T'_{Macro} : T'_{Macro}} \tag{22a}$$

$$\overline{T}^{VM}_{MicroRVE} = \sqrt{\frac{3}{2}T'_{Micro} : T'_{Micro}} \tag{22b}$$

where T'_{Macro} and T'_{Micro} are the deviatoric stresses of the volume averaged Cauchy stresses in the macro and micro RVE models, respectively, and the : operator symbolizes the double dot product of the two second order tensors. The difference between $\overline{T}^{VM}_{MacroRVE}$ and $\overline{T}^{VM}_{MicroRVE}$ are calculated and minimized using

$$\Delta = \overline{T}^{VM}_{MacroRVE} - \overline{T}^{VM}_{MicroRVE} \tag{23a}$$

$$\| \Delta \| = \sqrt{\Delta : \Delta}\,|_{min}\,. \tag{23b}$$

The computed von Mises stress for the macro RVE are reported in Table 3. The residual von Mises stress between the macro and micro RVE models was minimized to enforce consistency between both models and to ensure proper mapping to the down–scale model.

Table 3 The von Mises stress index ($\overline{T}^{VM}_{MacroRVE}$) used for macro-mico model coupling. Values are reported for both layers (Fibrosa–F, Ventricularis–V) in tension (+) and compression (−) and under inactive, normal and hypertensive states. Table adapted from [2]

Activation State	F+ (kPa)	F− (kPa)	V+ (kPa)	V− (kPa)
Inactive	4.58	3.08	3.46	2.76
Normal	6.92	3.29	4.90	2.89
Hyper	8.18	3.29	4.90	2.99

3.7 Micro Model Parameter Estimation

The AVIC cytoplasm stiffness (μ^{cyto}) and ECM stiffness ($\mu^{l,d}_{ECM}$) are defined as fixed values within the micro RVE model. Cytoplasm stiffness (μ^{cyto}) is set to 18 kPa based on AFM measurements performed on AVICs [33]. ECM stiffness ($\mu^{l,d}_{ECM}$) is computed using the tissue parameters determined from the macro RVE model for the inactive treatment group to systematically exclude contributions from either AVIC basal tonus or contraction. Using the rule of mixtures, the relation between ECM stiffness and AVIC cytoplasm stiffness is formulated as:

$$_{inactive}\mu^{l,d}_{Macro} = \mu^{l,d}_{ECM}\phi_{ECM} + \mu^{cyto}\phi_{AVIC} \tag{24}$$

where $_{inactive}\mu^{l,d}_{Macro}$ are the inactive layer tissue parameters from the macro RVE model and ϕ_{ECM} and ϕ_{AVIC} are the volume fractions of the ECM and AVICs set at 0.90 and 0.10, respectively. Using Eq. 24, the stiffness of the ECM for each layer under tension and compression (μ^{F+}_{ECM}, μ^{F-}_{ECM}, μ^{V+}_{ECM} and μ^{V-}_{ECM}) are determined and input into the micro RVE model.

After μ^{cyto} and $\mu^{l,d}_{ECM}$ are determined, the following parameters are estimated from the micro RVE model through the macro-micro coupling approach:

1. $_{state}\mu^{l,d}_{SF}$: Stress fiber stiffness
2. $_{state}f^{l,d}_{0}$: Stress fiber contraction strength
3. β^{l}_{AVIC} : AVIC connectivity to the ECM.

The remainder of this section describes the influence of each parameter.

3.7.1 The Effect of Stress Fiber Stiffness on the Micro RVE Response

The inactive state volume average von Mises stress in the fibrosa was used to evaluate the effect of the stress fiber shear modulus on tissue mechanical response. Stress fiber stiffness (μ_{sf}) is varied from 0–50 kPa and it is observed that this had little effect on the micro RVE model volume averaged von Mises stress (Fig. 9a). Therefore, μ_{sf} was determined to be 1 kPa from previous 2D microindentation studies and was fixed at this value for the remainder of the simulations.

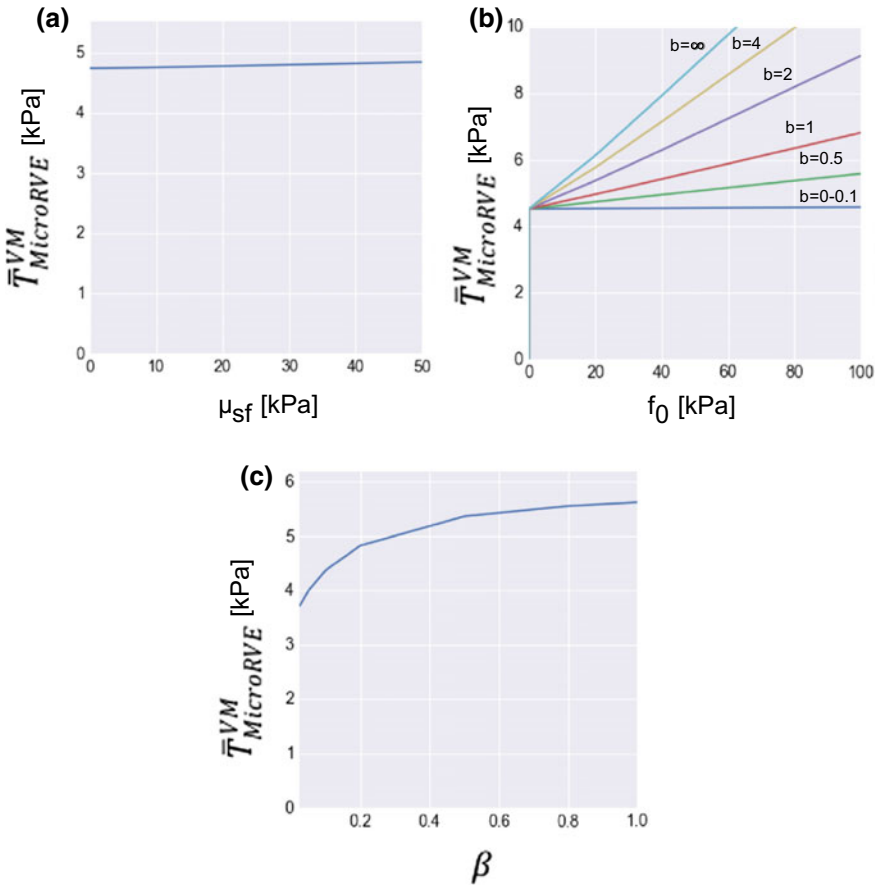

Fig. 9 **a** The stress fiber shear modulus (μ_{sf}) has little to no effect on $\overline{T}^{VM}_{MicroRVE}$. **b** The effect of the stress fiber orientation parameter b on $\overline{T}^{VM}_{MicroRVE}$. **c** The effect of the AVIC-ECM connectivity parameter β on the volume averaged von Mises stress. As connectivity increases, $\overline{T}^{VM}_{MicroRVE}$ increases as well. Figure taken from [2]

3.7.2 Determination of AVIC In-Situ Contraction Strength

To estimate the contraction strength, an appropriate stress fiber orientation parameter b is first determined. A parametric study of the parameter b is performed where the value for b is set to 0, 0.5, 1, 2, 4, and ∞ (Fig. 9b) for the fibrosa layer in the inactivated state. It was observed that when $b = 0$, the AVIC contraction did not contribute towards the von Mises stress of the micro RVE and it remained at 4.58 kPa as determined from the macro RVE (Table 3). As b increased, a linear trend between the contraction strength f_0 and $\overline{T}^{VM}_{MicroRVE}$ emerged. It is noted that as b increases, less contraction

Table 4 Parametric study of the parameter b. The contraction force required to match the RVE_{macro} von Mises stress decreased as b increased for both the normal and hypertensive cases

b	0	0.1	0.5	1	2	4	∞
f_0–normal [kPa]	N/A	N/A	223	105.5	52.1	35.1	27.4
f_0–hypter [kPa]	N/A	N/A	306	156.3	79.9	53.8	42.4

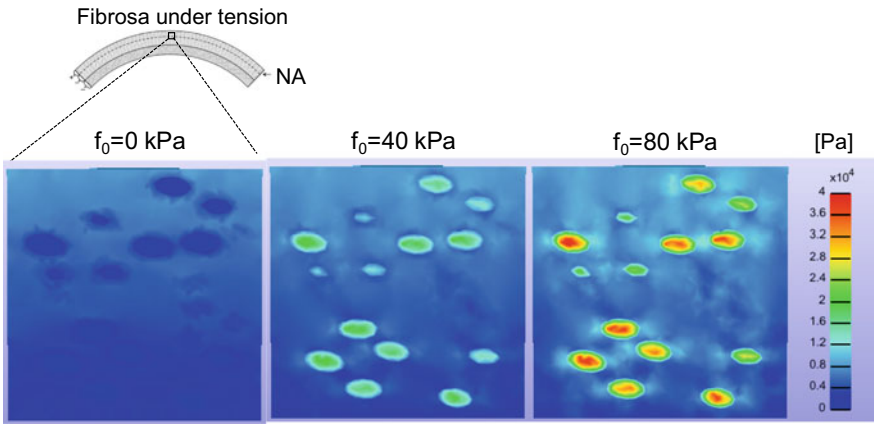

Fig. 10 The effect of AVIC contraction strength (f_0) on the surrounding von Mises stress of the ECM. Figure taken from [2]

force is needed to reach the same $\overline{T}^{VM}_{MicroRVE}$ (Table 4). This is because increasing b essentially increases the alignment of the 3D stress fiber orientation, allowing the AVIC inclusions to contribute in concert and as a result decrease the total level of f_0 needed per AVIC to reach the same outcomes.

From comparison of the π-periodic von Mises distribution with different b values to the constrained 2D von Mises distribution quantified previously [39, 40], a b value of 2.0 was chosen as the estimate of the 3D stress fiber orientation distribution. Shown in Table 4, f_0 = 52.1 and 79.9 kPa are used here on out for the normal and hypertensive simulations, respectively. With $b = 2.0$, simulations are implemented to assess how the magnitude of the contraction strength alters the surrounding ECM (Fig. 10). When the contraction strength is set to 0 kPa, the von Mises stress of the ECM is greater than that of the AVIC inclusions due to the lack of contraction. As contraction is increased to 40 and 80 kPa, the von Mises stress of the AVIC inclusions surpassed that of the ECM.

3.7.3 Layer-Specific AVIC-ECM Connectivity

With the b and f_0 parameters determined, the AVIC-ECM connectivity (β) within the ventricularis is estimated using Eq. 21. The β term is varied and the effect on

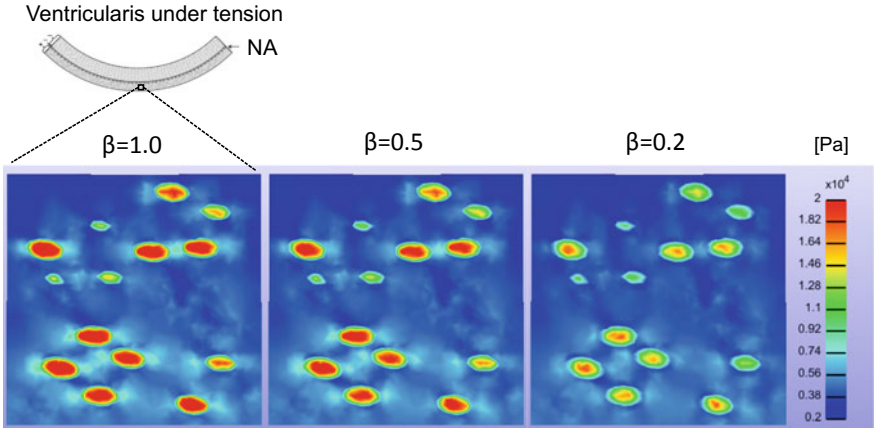

Fig. 11 The effect of AVIC-ECM connectivity (β) on the von Mises stress of the surrounding ECM. Figure taken from [2]

the resulting von Mises stress is plotted for the ventricularis under tension (Fig. 9c). Figure 9c, shows that a β value of 0.24 best matches the von Mises stress (4.90 kPa, Table 3), suggesting that the vetricularis is ~75% less connected than the fibrosa.

It is noted that as the value of β increases, the total von Mises stress increases as well (Fig. 11). This is because the mechanical connection between the AVICs and the ECM governs the net effect of AVIC contraction on the von Mises stress of the surrounding ECM. Not only does the von Mises stress within the AVIC inclusions increase due to an increase in connectivity, but the von Mises stress of the immediately surrounding ECM also increases.

3.8 Differences in Cell Total Traction Forces in 2D Versus 3D

To better understand the difference in AVIC biophysical state in 2D vs 3D, the total force generated by each individual AVIC is computed through the expression

$$F_{tot} = \int_{\Gamma} |T(x)| dA \tag{25}$$

where Γ represents the boundary of the AVIC inclusions and $T(x)$ is the traction along the boundary. It is found that in-situ, AVICs generate 0.2 and 0.35 μN of force in the normal and hypertensive states, respectively. This is more than twice the force that is generated by AVICs seeded on 2D substrates as determined from microindentation studies (normal = 0.07 μN and hypertensive = 0.16 μN) [40]. The average traction force over the boundary is computed as

$$T_{avg} = \frac{1}{SA} \int_{\Gamma} |T(x)| dA. \tag{26}$$

In-situ, the average traction over the AVIC boundary is 429 Pa and 752 Pa for the normal and hypertensive states, respectively. In the 2D micro-indentation studies, the average traction over the boundary is computed as 300 and 450 pa for the normal and hypertensive state, respectively, which is substantially lower than what was found for AVICs in-situ.

3.9 Conclusions

The insights gained from the isolated cell studies were successfully incorporated into a more physiologically relevant model of the AVIC in-situ. From the macro-micro modelling approach, the total force and average traction of the AVICs in-situ is determined. In 3D, AVICs generate greater total and average forces per unit area. This is hypothesized to be driven by the increased attachment sites available in 3D compared to 2D cultures.

The layer-specific connectivity of the AVICs is also estimated. Most notably, AVICs within the ventricularis are estimated to be ∼75% less connected to the ECM than AVICs in the fibrosa. This offers a possible explanation as to why no significant change in E_{eff} was observed from the AV bending experiments when the AVICs were in a hypertensive state and the AV test specimens were bent in the WC direction (ventricularis under tension) (Fig. 6b). In contrast, the AVICs in the fibrosa layer are predicted to be more connected to the ECM which potentially explains the significant increase in E_{eff} observed when the AV leaflets are tested in the AC direction under hypertensive treatments.

The macro-micro model of the AV leaflet described here should be considered a first pass towards modeling in-situ AVIC mechanical behavior. Recent advances in micromechanical continuum mechanics offers a potential strategy to solve the micro RVE model analytically which will reduce computational costs [35]. In the future, the model should also be refined to include realistic cell geometries, and incorporate the separate contributions of the stress fiber networks (namely α-SMA and F-actin). In addition, future efforts should also focus on modeling the structural differences between the fibrosa and ventricularis layers.

4 An Approach to Studying VIC Mechanobiology Using Tunable Hydrogels

4.1 Overview

The majority of VIC mechanical and mechanobiological studies have been performed either on 2D substrates or in suspension. Although insightful, these techniques vastly

underestimate the complexity of the native heart valves and do not recapitulate the in-vivo cell environment. Using native tissue for experimentation offers an alternative to 2D cultures but is also limited in that they cannot be tuned to answer specific mechanobiological questions nor can the subcellular components of the AVICs be directly and conveniently visualized. In response to these limitations, synthetic hydrogels have recently grown in popularity as an alternative method to study cells within highly tunable and transparent 3D environments. Synthetic hydrogels also open up the possibility of conducting high-throughput studies using healthy and diseased VICs isolated from human tissue samples. Studies have been conducted to assess AVIC contractile responses within peptide-modified, poly (ethylene glycol) (PEG) hydrogels [22] and are summarized in this section.

4.2 Experimental Methods

4.2.1 AVIC-Hydrogel Fabrication

Porcine AVICs were suspended in a hydrogel pre-cursor solution consisting of norbornene-functionalized PEG, matrix metalloproteinase (MMP)-degradable crosslinking peptides, CRGDS adhesive peptides, lithium phenyl- 2,4,6 -trimethylbenzolphosphinate photoinitiator, and PBS at a concentration of 10 millions cells/ml. The cell seeded hydrogel polymer solution was then pipetted into 10 × 5 mm molds and AVIC-hydrogels were cured under UV light for 3 min (Fig. 12). The amount of MMP-degradable crosslinks and CRGDS peptides were tuned to study the effect of hydrogel stiffness and adhesive ligand density, respectively, on AVIC contraction.

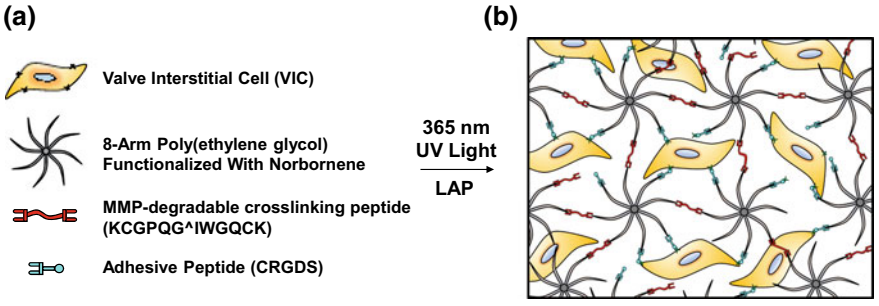

Fig. 12 **a** The components of the hydrogel pre-cursor solution. **b** Schematic of the theorized AVIC-hydrogel internal structure. Figure taken from [22]

4.2.2 End-Loading, Flexural Deformation Testing

Similar to the bending tests performed on native AV leaflets [32], the AVIC hydrogels were subjected to repeated flexural deformation tests after treatment with 5 mM KCl (normal), 90 mM KCl (hypertensive), and 70% methanol (inactive) for a total of three flexural tests per specimen (Fig. 13).

The Euler-Bernoulli relation was used for analysis. The change in curvature of the specimen ($\Delta\kappa$) was computed using the position of the fiducial markers. The moment (M) at the center of the specimen was computed as:

$$M = P * y \tag{27}$$

where P is the end-loading force required to bend the specimen and y is the deflection of the center marker in the y-direction. From these calculations, moment versus curvature plots were generated for the AVIC-hydrogel specimens (Fig. 14).

4.3 Finite Element Modeling

From the experimental data, it was observed that the moment-curvature plots for the AVIC hydrogels were consistently non-linear (Fig. 14). This causes E_{eff} to be non-constant and a function of the change in curvature. This posed difficulty towards selecting an appropriate E_{eff} to compare between hydrogel groups with both different compositions and different contractile states of the underlying AVICs. To mitigate this, a finite element model of the bending experiment was developed in FEniCS

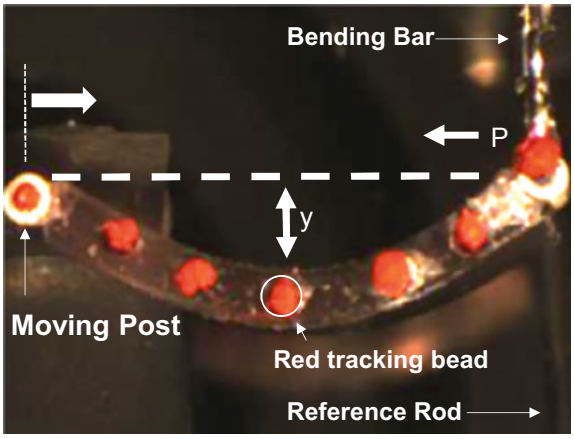

Fig. 13 Flexural deformation testing of an AVIC-hydrogel. Red fiducial markers were placed along the length of the hydrogel to track the deformation of the test specimen. Figure taken from [22]

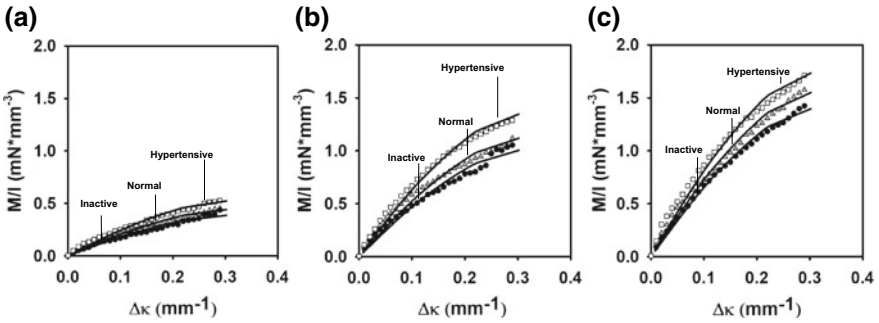

Fig. 14 Experimental (dotted line) and simulated (solid line) moment versus curvature plots for **a** 2.5, **b** 5, and **c** 10 kPa hydrogels under normal, hypertensive, and inactive conditions. Figure taken from [22]

[27, 28], and the AVIC-hydrogels were modeled with a neo-Hookean material model with the following strain energy density function:

$$W = \frac{\mu}{2}(I_1 - 3) + \frac{1}{2}K(J-1)^2 \tag{28}$$

where μ serves as a convenient material parameter to compare between hydrogel groups and contractile levels and is the large deformation equivalent of the shear modulus and K is the bulk modulus of the material. To enforce incompressibility, $K = \mu * 10{,}000$ and the change in volume ratio was subsequently confirmed to be insignificant. Shear modulus (μ) was determined using a gradient descent algorithm to minimize the least-square errors between the simulated and experimental moment vs curvature data (Fig. 14).

4.4 Modeling Results

The percent change in μ from the inactive to the normal state and from the inactive to the hypertensive state is reported for both the stiffness modulated and CRGDS adhesive peptide modulated AVIC-hydrogels in Fig. 15.

In the stiffness modulated group, AVICs seeded within 2.5 kPa gels displayed a larger change in stiffness from the inactive to the normal condition and from the inactive to the hypertensive condition than in the 5 and 10 kPa gels (Fig. 15a). This may be due to an increase in AVIC activation within softer hydrogels and the development of prominent α-SMA fiber networks that are seen in the fluorescent images discussed in the next section (Fig. 16). A higher percent change in μ from the inactive condition to the normal condition within the 2.5 kPa gels suggests that the basal tonus of the AVICs contributes more to the overall construct stiffness than in

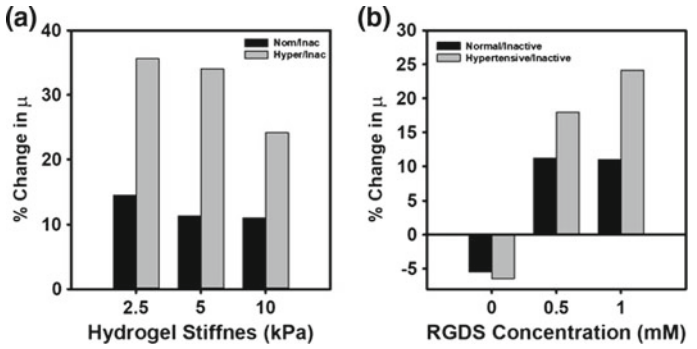

Fig. 15 **a** The percent change in μ for the stiffness modulated AVIC-hydrogels. **b** The percent change in μ for AVIC-hydrogels with varying levels of CRGDS adhesive peptide concentration. Figure adapted from [22]

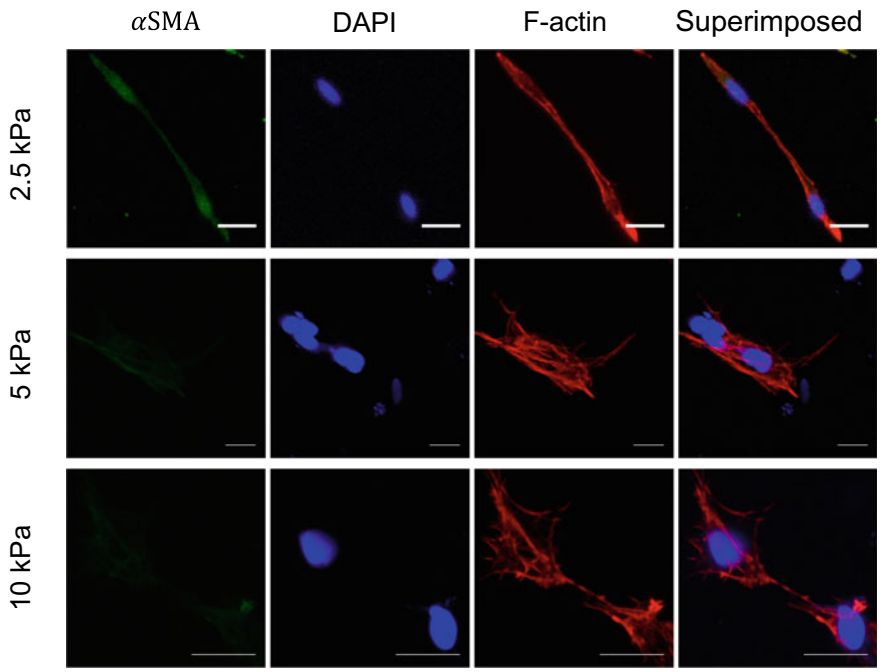

Fig. 16 Subcellular AVIC structures imaged directly within the hydrogel using confocal microscopy (scale bar = 20 μm). Figure taken from [22]

the higher stiffness hydrogels. Notably, the AVICs in the 5 kPa gels produce a larger change in μ in the hypertensive state than in the 10 kPa gels. However, the basal tonus (inactive to normal state) remained the same between the two groups.

As CRGDS concentration increased, the effect of AVIC contraction on the hydrogel construct flexural stiffness increased as well (Fig. 15b). The most prominent effects were observed in the 1 mM CRGDS group followed by the 0.5 mM CRGDS group. In the 0 mM CRGDS group, AVIC contraction had no positive effect towards the construct flexural stiffness.

4.5 Visualization of AVIC Cellular Structures Directly Within the Hydrogel Environment

A separate group of AVIC-hydrogels were stained for α-SMA fibers, the nucleus (DAPI stain), and F-actin fibers and visualized using confocal microscopy (Fig. 16). AVICs seeded within softer hydrogels seemed to elongate more than in higher stiffness hydrogels. In addition, AVICs within 2.5 kPa gels displayed detectable α-SMA expression whereas AVICs within 5 and 10 kPa gels did not. This potentially explains the larger influence of AVIC contraction on hydrogel construct flexural stiffness within the 2.5 kPa group. Complex F-actin fiber networks were present within AVICs among all hydrogel stiffness groups.

4.6 Conclusions

AVICs establish significant mechanical coupling to the synthetic hydrogel environment and can effect the overall flexural stiffness of these constructs. The gel system is an extremely attractive tool for future mechanobiological studies involving mechanical conditioning of the AVIC-hydrogels within uniaxial and biaxial stretch bioreactors. Current work is underway to use the gel system to study the effects of cyclic uniaxial loading on human AVICs from healthy patients and those with bicuspid AVs to investigate the effects of cell deformation in a 3D microenvironment on AVIC biosynthesis. This is a first pass attempt at modeling the macro level respose of cell seeded hydrogels in bending. Future work will focus on incorporating the explicit contraction effects of AVICs within the hydrogel through adapting the current AV leaflet macro-micro modeling approach to the hydrogel system and utilizing the transparency of the gels to inform the model with realistic cell and stress fiber geometries.

5 Future Directions

5.1 Modeling of VIC Cell Signaling Pathways

The macro-micro modeling approach described in Sect. 3 uses the parameter β^{l}_{AVIC} to describe the degree of connectivity between the AVIC and the ECM and this approach has been able to describe some key aspects of how VICs sense their surrounding ECM. However, a mechanistic view that couples the binding of AVIC receptors to the ECM and how these events propagate to altered transcription is lacking. Therefore, future research will be directed toward elucidating the intracellular mechanotransduction pathways that allow VICs to sense and respond to altered ECM concentrations and mechanical stimuli via mathematical modeling.

As the major receptors that allow cells to adhere to substrates such as ECM, integrins are key players in VIC mechanotransduction processes. In addition to binding the ECM, integrins also bind a variety of adapter proteins that provide a structural link to the actin cytoskeleton, connecting external and internal cellular forces. This structural linkage has been described as a "mechanical clutch" and was initially modeled by Chan and Odde [6] and has been recently extended by others (e.g., [11, 16, 47]). These models explicitly incorporate the force on the ECM-integrin-adapter-actin structural linkage through force-dependent bond lifetimes and the unveiling of binding sites for structural reinforcement in the adapter. These models are able to relate substrate rigidity to the maturity of focal adhesion structures developed.

In addition to their structural properties, integrins also signal through proteins such as focal adhesion kinase (FAK). FAK interacts with many downstream pathways, including (a) Rho/Rac signaling to alter the actin cytoskeleton [24], (b) Ras/ERK pathways to dismantle focal adhesions [41], and (c) PI3K/Akt pathways to facilitate the myofibroblast transition and αSMA production [9, 45]. These "pathways" are not linear cascades; rather, they are influenced by many cross-talk mechanisms, instead creating a complex signaling network.

The complexity of this integrin-mediated signaling network obfuscates the role of individual proteins in overall VIC phenotypic transitions. However, reconstructing these pathways through mathematical modeling can provide information on the most influential states or parameters governing these transitions, directing future experiments. Furthermore, such a model can be used to influence cellular biomechanics models within a multiscale framework.

5.2 A Flexible and Extensible 3D Multi-scale Computational Modeling Framework

Future computational research will be geared towards robust mechanistic modeling of the VICs seeded in the 3D hydrogel systems described in Sect. 4. The tunable hydrogel system and the multi-scale, multi-resolution modeling framework will work

in concert to elucidate experimentally observed cell and system behavior and ultimately aid in comparing between the synthetic and native VIC environments. Direct enhancements to the VIC-ECM model described in Sect. 3 include the implementation of a more realistic cellular geometry, implementation of additional sub-cellular features such as cell nuclei, a more complex strategy for capturing the cell-ECM attachment zone, and the consideration of aleatoric uncertainty. With regard to the ECM fiber network, sub-cellular scale mechanism based material models for ECM and cell cytoplasm remodeling will be explored [14]. Finally, integrating aspects of the cell signaling models described in Sect. 5.1 into the finite element framework will offer a controllable platform to explore potential non-linearities and feedback loops that rely on spatial information.

With this significant added model complexity, model interpretability will suffer. And, more computationally expensive models will pose feasibility challenges for robust simulations at larger spatial scales. To mitigate this, novel strategies for model interpretability are required [25]. One key strategy will be defining experimentally relevant quantities of interest, and running global sensitivity analysis to understand the relative contributions of different model input parameters [18, 26, 42]. Another key strategy will be developing and incorporating appropriate methods for multi-scale and multi-resolution model integration. Looking forward, the computational model and associated techniques developed to meet these challenges should be extensible to modeling other experimental systems.

References

1. Acker, M.A., Parides, M.K., Perrault, L.P., Moskowitz, A.J., Gelijns, A.C., Voisine, P., Smith, P.K., Hung, J.W., Blackstone, E.H., Puskas, J.D.: Mitral-valve repair versus replacement for severe ischemic mitral regurgitation. N. Engl. J. Med. **370**(1), 23–32 (2014)
2. Buchanan, R.M.: A An integrated computational-experimental approach for the in situ estimation of valve interstitial cell biomechanical state. Doctoral Thesis. The University of Texas at Austin (2016). https://repositories.lib.utexas.edu/handle/2152/39463
3. Buchanan, R.M., Sacks, M.S.: Interlayer micromechanics of the aortic heart valve leaflet. Biomech Model Mechanobiol (2013). https://doi.org/10.1007/s10237-013-0536-6. http://www.ncbi.nlm.nih.gov/pubmed/24292631
4. Butcher, J.T., Simmons, C.A., Warnock, J.N.: Mechanobiology of the aortic heart valve. J. Heart Valve. Dis. **17**(1), 62–73 (2008). http://www.ncbi.nlm.nih.gov/entrez/query.fcgi?cmd=Retrieve&db=PubMed&dopt=Citation&list_uids=18365571
5. Carruthers, C.A., Alfieri, C.M., Joyce, E.M., Watkins, S.C., Yutzey, K.E., Sacks, M.S.: Gene Expression and Collagen Fiber Micromechanical Interactions of the Semilunar Heart Valve Interstitial Cell. Cell. Mol. Bioeng. **5**(3), 254–265 (2012). https://doi.org/10.1007/s12195-012-0230-2
6. Chan, C.E., Odde, D.J.: Traction dynamics of filopodia on compliant substrates. Science **322**(5908), 1687–1691 (2008). https://doi.org/10.1126/science.1163595
7. Chaput, M., Handschumacher, M.D., Guerrero, J.L., Holmvang, G., Dal-Bianco, J.P., Sullivan, S., Vlahakes, G.J., Hung, J., Levine, R.A.: Mitral leaflet adaptation to ventricular remodeling: prospective changes in a model of ischemic mitral regurgitation. Circulation **120**(11 Suppl), S99–103 (2009). https://doi.org/10.1161/CIRCULATIONAHA.109.844019. http://www.ncbi.nlm.nih.gov/pubmed/19752393

8. Chaput, M., Handschumacher, M.D., Tournoux, F., Hua, L., Guerrero, J.L., Vlahakes, G.J., Levine, R.A.: Mitral leaflet adaptation to ventricular remodeling: occurrence and adequacy in patients with functional mitral regurgitation. Circulation **118**(8), 845–52 (2008). https://doi.org/10.1161/circulationaha.107.749440. http://circ.ahajournals.org/content/118/8/845.full.pdf
9. Chen, H.C., Appeddu, P.A., Isoda, H., Guan, J.L.: Phosphorylation of tyrosine 397 in focal adhesion kinase is required for binding phosphatidylinositol 3-kinase. J. Biol. Chem. **271**(42), 26329–26334 (1996). https://doi.org/10.1074/jbc.271.42.26329
10. Chen, J., Li, H., SundarRaj, N., Wang, J.H.: Alpha-smooth muscle actin expression enhances cell traction force. Cell Motil Cytoskelet. **64**(4), 248–57 (2007). https://doi.org/10.1002/cm.20178. http://www.ncbi.nlm.nih.gov/pubmed/17183543
11. Cheng, B., Lin, M., Li, Y., Huang, G., Yang, H., Genin, G.M., Deshpande, V.S., Lu, T.J., Xu, F.: An integrated stochastic model of matrix-stiffness-dependent filopodial dynamics. Biophys. J. **111**(9), 2051–2061 (2016). https://doi.org/10.1016/j.bpj.2016.09.026
12. Clark-Greuel, J.N., Connolly, J.M., Sorichillo, E., Narula, N.R., Rapoport, H.S., Mohler 3rd, E.R., Gorman 3rd, J.H., Gorman, R.C., Levy, R.J.: Transforming growth factor-beta1 mechanisms in aortic valve calcification: increased alkaline phosphatase and related events. Ann. Thorac. Surg. **83**(3), 946–53 (2007). https://doi.org/10.1016/j.athoracsur.2006.10.026. http://www.ncbi.nlm.nih.gov/pubmed/17307438
13. Cushing, M.C., Liao, J.T., Anseth, K.S.: Activation of valvular interstitial cells is mediated by transforming growth factor-beta1 interactions with matrix molecules. Matrix Biol. **24**(6), 428–37 (2005). http://www.ncbi.nlm.nih.gov/entrez/query.fcgi?cmd=Retrieve&db=PubMed&dopt=Citation&list_uids=16055320
14. Deshpande, V.S., Mrksich, M., McMeeking, R.M., Evans, A.G.: A bio-mechanical model for coupling cell contractility with focal adhesion formation. J. Mech. Phys. Solids **56**(4), 1484–1510 (2008)
15. Edman, K.A.: The relation between sarcomere length and active tension in isolated semitendinosus fibres of the frog. J. Physiol. **183**(2), 407–17 (1966). http://www.ncbi.nlm.nih.gov/pubmed/5942818
16. Elosegui-Artola, A., Oria, R., Chen, Y., Kosmalska, A., Pérez-González, C., Castro, N., Zhu, C., Trepat, X., Roca-Cusachs, P.: Mechanical regulation of a molecular clutch defines force transmission and transduction in response to matrix rigidity. Nat. Cell Biol. **18**(5), 540–548 (2016). https://doi.org/10.1038/ncb3336
17. Gouget, C.L., Girard, M.J., Ethier, C.R.: A constrained von Mises distribution to describe fiber organization in thin soft tissues. Biomech Model Mechanobiol **11**(3–4), 475–82 (2012). https://doi.org/10.1007/s10237-011-0326-y. http://www.ncbi.nlm.nih.gov/pubmed/21739088
18. Hart, J., Alexanderian, A., Gremaud, P.: Efficient computation of sobol' indices for stochastic models. SIAM J. Sci. Comput. **39**(4), 1514–1539 (2017)
19. Hinz, B., Phan, S.H., Thannickal, V.J., Prunotto, M., Desmouliere, A., Varga, J., De Wever, O., Mareel, M., Gabbiani, G.: Recent developments in myofibroblast biology: paradigms for connective tissue remodeling. Am J Pathol **180**(4), 1340–55 (2012). https://doi.org/10.1016/j.ajpath.2012.02.004. http://www.ncbi.nlm.nih.gov/pubmed/22387320
20. Huang, H.Y., Liao, J., Sacks, M.S.: In-situ deformation of the aortic valve interstitial cell nucleus under diastolic loading. J Biomech Eng **129**(6), 880–89 (2007). https://doi.org/10.1115/1.2801670. http://www.ncbi.nlm.nih.gov/entrez/query.fcgi?cmd=Retrieve&db=PubMed&dopt=Citation&list_uids=18067392
21. Khalighi, A.H., Drach, A., Bloodworth, C.H., Pierce, E.L., Yoganathan, A.P., Gorman, R.C., Gorman, J.H., Sacks, M.S.: Mitral valve chordae tendineae: Topological and geometrical characterization. Ann. Biomed. Eng. **45**, 378–393 (2017). https://doi.org/10.1007/s10439-016-1775-3
22. Khang, A., Gonzalex, A.G., Schroeder, M.E., Sansom, J., Anseth, K.S., Sacks, M.S.: An approach to quantify valve interstitial cell biophysical state using highly tunable poly(ethylene) glycol hydrogels. Manuscript in preparation (2018)
23. Latif, N., Sarathchandra, P., Taylor, P., Antoniw, J., Yacoub, M.: Molecules mediating cell-ECM and cell-cell communication in human heart valves. Cell Biochemistry and Biophysics **43**(2), 275–287 (2005). https://doi.org/10.1385/CBB:43:2:275

24. Lawson, C.D., Burridge, K.: The on-off relationship of Rho and Rac during integrin-mediated adhesion and cell migration. Small GTPases **5**(1), e27958 (2014). https://doi.org/10.4161/sgtp.27958
25. Lejeune, E., Linder, C.: Quantifying the relationship between cell division angle and morphogenesis through computational modeling. J. Theor. Biol. **418**, 1–7 (2017)
26. Lejeune, E., Linder, C.: Understanding the relationship between cell death and tissue shrinkage via a stochastic agent-based model. J. Biomech. **73**, 9–17 (2018)
27. Logg, A., Mardal, K.A., Wells, G.: Automated Solution of Differential Equations by the Finite Element Method the FEniCS Book, 2012. edn. Lecture Notes in Computational Science and Engineering,. Springer Berlin Heidelberg, Berlin, Heidelberg (2012). http://UTXA.eblib.com/patron/FullRecord.aspx?p=885214
28. Logg, A., Wells, G.N.: DOLFIN: Automated Finite Element Computing. Acm Transactions on Mathematical Software **37**(2) (2010). https://doi.org/10.1145/1731022.1731030. http://WOS:000277057400008
29. Maas, S., Rawlins, D., Weiss, J., Weiss, J.: FEBio User's Manual Version 2.4 (2015). http://febio.org/download/febio-2-4-users-manual/
30. Maas, S.A., Ellis, B.J., Ateshian, G.A., Weiss, J.A.: FEBio: finite elements for biomechanics. J Biomech Eng **134**(1), 011005 (2012). https://doi.org/10.1115/1.4005694. http://www.ncbi.nlm.nih.gov/pubmed/22482660
31. Merryman, W.D.: Mechanobiology of the aortic valve interstitial cell. Doctoral Dissertation, University of Pittsburgh, Doctoral Dissertation (2007)
32. Merryman, W.D., Huang, H.Y.S., Schoen, F.J., Sacks, M.S.: The effects of cellular contraction on aortic valve leaflet flexural stiffness. J Biomech **39**(1), 88–96 (2006). http://www.ncbi.nlm.nih.gov/entrez/query.fcgi?cmd=Retrieve&db=PubMed&dopt=Citation&list_uids=16271591
33. Merryman, W.D., Liao, J., Parekh, A., Candiello, J.E., Lin, H., Sacks, M.S.: Differences in tissue-remodeling potential of aortic and pulmonary heart valve interstitial cells. Tissue Eng. **13**(9), 2281–9 (2007). http://www.ncbi.nlm.nih.gov/entrez/query.fcgi?cmd=Retrieve&db=PubMed&dopt=Citation&list_uids=17596117
34. Merryman, W.D., Youn, I., Lukoff, H.D., Krueger, P.M., Guilak, F., Hopkins, R.A., Sacks, M.S.: Correlation between heart valve interstitial cell stiffness and transvalvular pressure: implications for collagen biosynthesis. Am. J. Physiol. Heart Circ. Physiol. **290**(1), H224–31 (2006). http://www.ncbi.nlm.nih.gov/entrez/query.fcgi?cmd=Retrieve&db=PubMed&dopt=Citation&list_uids=16126816
35. Morin, C., Avril, S., Hellmich, C.: Non-affine fiber kinematics in arterial mechanics: a continuummicromechanical investigation. J. Appl. Math. Mech. (2018)
36. Osman, L., Yacoub, M.H., Latif, N., Amrani, M., Chester, A.H.: Role of human valve interstitial cells in valve calcification and their response to atorvastatin. Circulation **114**(1 Suppl), 1547–1552 (2006). http://www.ncbi.nlm.nih.gov/entrez/query.fcgi?cmd=Retrieve&db=PubMed&dopt=Citation&list_uids=16820635
37. Rego, B.V., Sacks, M.S.: A functionally graded material model for the transmural stress distribution of the aortic valve leaflet. J. Biomech. **54**, 88–95 (2017). https://doi.org/10.1016/j.jbiomech.2017.01.039
38. Rego, B.V., Wells, S.M., Lee, C.H., Sacks, M.S.: Mitral valve leaflet remodelling during pregnancy: insights into cell-mediated recovery of tissue homeostasis. J. R. Soc., Interface **13**(125) (2016). https://doi.org/10.1098/rsif.2016.0709. http://rsif.royalsocietypublishing.org/content/13/125/20160709
39. Sakamoto, Y., Buchanan, R.M., Sacks, M.S.: On intrinsic stress fiber contractile forces in semilunar heart valve interstitial cells using a continuum mixture model. J Mech Behav Biomed Mater **54**, 244–58 (2016). https://doi.org/10.1016/j.jmbbm.2015.09.027. http://www.ncbi.nlm.nih.gov/pubmed/26476967
40. Sakamoto, Y., Buchanan, R.M., Sanchez-Adams, J., Guilak, F., Sacks, M.S.: On the functional role of valve interstitial cell stress fibers: a continuum modeling approach. J. Biomech. Eng. **139**, (2017). https://doi.org/10.1115/1.4035557

41. Schlaepfer, D.D., Hanks, S.K., Hunter, T., van der Geer, P.: Integrin-mediated signal transduction linked to Ras pathway by GRB2 binding to focal adhesion kinase. Nature **372**, 786–791 (1994). https://doi.org/10.1038/372786a0
42. Sobol, I.: Global sensitivity indices for nonlinear mathematical models and their monte carlo estimates. Math. Comput. Simul. **55**(1), 271–280 (2001)
43. Stephens, E., Durst, C., Swanson, J., Grande-Allen, K., Ingels, N., Miller, D.: Functional Coupling of Valvular Interstitial Cells and Collagen Via a2b1 Integrins in the Mitral Leaflet. Cell Mol. Bioeng. pp. 1–10 (2010). https://doi.org/10.1007/s12195-010-0139-6
44. Vernerey, F.J., Farsad, M.: A constrained mixture approach to mechano-sensing and force generation in contractile cells. J. Mech. Behav. Biomed. Mater. **4**(8), 1683–1699 (2011). https://doi.org/10.1016/j.jmbbm.2011.05.022. http://WOS:000298764700012
45. Wang, H., Tibbitt, M.W., Langer, S.J., Leinwand, L.A., Anseth, K.S.: Hydrogels preserve native phenotypes of valvular fibroblasts through an elasticity-regulated PI3K/AKT pathway. Proc. Natl. Acad. Sci. **110**(48), 19336–19341 (2013). https://doi.org/10.1073/pnas.1306369110
46. Wang, J., Zohar, R., McCulloch, C.A.: Multiple roles of alpha-smooth muscle actin in mechanotransduction. Exp. Cell Res. **312**(3), 205–14 (2006). http://www.ncbi.nlm.nih.gov/entrez/query.fcgi?cmd=Retrieve&db=PubMed&dopt=Citation&list_uids=16325810
47. Welf, E.S., Johnson, H.E., Haugh, J.M.: Bidirectional coupling between integrin-mediated signaling and actomyosin mechanics explains matrix-dependent intermittency of leading-edge motility. Mol. Biol. Cell **24**(24), 3945–3955 (2013). https://doi.org/10.1091/mbc.e13-06-0311